Biochimica et Biophysica Acta 1848 (2015) 859–868

Contents lists available at ScienceDirect

Biochimica et Biophysica Acta

journal homepage: www.elsevier.com/locate/bbamem

Migration mechanism of mesenchymal stem cells studied by QD/NSOM

Changhong Ke [a], Jianan Chen [a], Yajun Guo [c], Zheng W. Chen [b], Jiye Cai [a,*]

[a] Department of Chemistry, Jinan University, Guangzhou 510632, China
[b] Department of Microbiology and Immunology, Center for Primate Biomedical Research, University of Illinois College of Medicine, Chicago, IL 60612, USA
[c] International Joint Cancer Institute and E-institutes of Shanghai Universities Immunology Division, The Second Military Medical University, Shanghai 200433, China

ARTICLE INFO

Article history:
Received 9 September 2014
Received in revised form 10 December 2014
Accepted 12 December 2014
Available online 19 December 2014

Keywords:
NSOM
QD
Mesenchymal stem cell
VEGF
CD44
CD29

ABSTRACT

The migration of mesenchymal stem cells (MSCs) plays a key role in tumor-targeted delivery vehicles and tumor-related stroma formation. However, there so far has been no report on the distribution of cell surface molecules during the VEGF-induced migration of MSCs. Here, we have utilized near-field scanning optical microscopy (NSOM) combined with fluorescent quantum dot (QD)-based nano-technology to capture the functional relationship between CD44 and CD29 adhesion molecules on MSCs and the effect of their spatial rearrangements. Before VEGF-induced migration of MSCs, both CD44 and CD29 formed 200–220 nm nano-domains respectively, with little co-localization between the two types of domains. Surprisingly, the size of the CD44 nano-domain rapidly increased in size to 295 nm and apparently larger aggregates were formed following MSC treatment with VEGF for 10 min, while the area of co-localization increased to 0.327 μm^2. Compared with CD44, CD29 was activated obviously later, for the fact that CD29 aggregation didn't appear until 30 min after VEGF treatment. Consistently, its co-localization area increased to 0.917 μm^2. The CD44 and CD29 nano-domains further aggregated into larger nano-domains or even formed micro-domains on the membrane of activated MSCs. The aggregation and co-localization of these molecules promoted FAK formation and cytoskeleton rearrangement. All of the above changes induced by VEGF contributed to MSC migration. Taken together, our data of NSOM-based dual color fluorescent imaging demonstrated for the first time that CD44, together with CD29, involved in VEGF-induced migration of MSCs through the interaction between CD44 and its co-receptor of VEGFR-2.

1. Introduction

Mesenchymal stem cells (MSCs) have the ability to self-renew and can be isolated and expanded from bone marrow and other tissues. MSCs that are positive for the markers CD105, CD90, CD73, CD44, CD166 and CD29 are multi-potent progenitors for several mesenchymal lineages, including osteoblasts, chondrocytes, adipocytes, myotubes and hematopoietic-supporting cells [1–3]. The ability of MSCs to self-renew and differentiate makes them a promising tool for clinical applications in regenerative medicine and tissue engineering [4–8]. The building of new blood vessels, or neovascularization, is a primary concern in a wide range of diseases. For example, area of interest in which MSCs are actively being studied is in the treatment of myocardial infarctions. To repair the region of infarction, MSCs must travel from the injection point to reach the target area [7,9–12]. Therefore, the common hypothesis is that MSCs possess migratory activity. Indeed, it has been reported that cytokines can stimulate MSC migration and support the potential of MSCs as tumor-targeted delivery vehicles for therapeutic agents by making use of these cytokines from tumors [13–16]. There is ample evidence to suggest that MSCs can be recruited to the location of tumors and can contribute to tumor-related stroma formation [2,17–21]. In addition, a number of studies have found that MSCs can migrate to regions of gastric carcinoma, melanoma, multiple myeloma and breast cancer [2,15,18,22].

Since directed migration of MSCs has important roles in both tumor-related stroma formation and in the role of MSCs as tumor-targeted delivery vehicles for therapeutic agents, understanding the precise mechanism underlying the tropism of MSCs induced by tumors has been an area of active study in recent years. For example, directed migration of MSCs to tumor sites can be mediated by several tumor-derived cytokines, including monocyte chemotactic protein-1 (MCP-1) [13], platelet derived growth factor [14], matrix metalloproteinase 1 [23] chemokine CCL25 [15], vascular endothelial growth factor (VEGF) [24], and basic fibroblast growth factor (FGF-basic) [7]. Among these cytokines, VEGF seems to be particularly important in enhancing and directing human MSC motility [7,25,26]. Although these views are confirmed by traditional method of biology, little is known about the specific molecular mechanisms involved in the VEGF-induced directed migration of MSCs.

Most recently, Aldridge et al. [27] reported that hMSCs migrate to liver tissues and endothelium and bind in greater numbers in disease conditions regulated by CD29 and CD44 in vitro and in vivo. CD29

* Corresponding author.

http://dx.doi.org/10.1016/j.bbamem.2014.12.013
0005-2736/

(β1-integrin) is a member of the integrin family that is responsible for mediating adhesion between the cell and the extracellular matrix. CD44 class I transmembrane glycoproteins are adhesion molecules involved in cell–cell and cell–substrate interactions. Some studies suggest that CD44 plays a key role in cytoskeletal rearrangement [28], takes part in a CD44–Src–integrin signaling axis in lipid rafts [29], and most importantly, CD44 can be a co-receptor of VEGFR-2 [30]. Direct visualization of the spatial distribution of CD29 and CD44 on the cell membrane and their changes during MSC activation with VEGF may help to elucidate the molecular mechanisms underlying the directional migration of MSC. However, these types of molecular imaging studies have not been reported.

Various methods have been employed to visualize the cell surface at nanometer scale resolution. For example, scanning tunneling microscopy (STM) can be used to visualize the cell surface at the highest resolution, but sample preparation can be complex. Atomic force microscopy (AFM) is limited for failing to obtain specific fluorescence information for naturally unknown molecules on cell surface. Laser scanning confocal microscopy does not provide sufficiently high resolution for the detection of cell membrane fluctuations and cell surface molecules at a nanometer scale [31]. Stimulated emission depletion (STED) and photoactivatable localization microscopy (PALM) lack simultaneous topographic information [32]. In contrast, NSOM is a microscopic technique where a sub-wavelength-sized aperture probe is raster scanned very close (<10 nm) to the sample, providing simultaneous optical and topographic lateral resolution beyond the diffraction limit of light [33]. Moreover, quantum dots (QDs) are a new class of fluorescent markers for immunofluorescent labeling and possess very high levels of brightness and photo-stability. As such, NSOM used in conjunction with QDs is the best technique by which the distribution of membrane receptors can be measured at the nanometer scale [31–37]. In this study, our results indicate that VEGF can induce directed migration of MSCs through the formation of (focal adhesion kinase) FAK and cytoskeletal rearrangements. To determine whether directed MSC migration is based on these adhesion molecules, we have developed the a NSOM/QDs-based nanotechnology using dual-color imaging to visualize the nanometer scale distribution and organization of CD44 and CD29, as well as their spatial organization on the cell surface. We found that VEGF can induce CD44 and CD29 molecules to form large clusters and much more CD44 molecules colocalize with CD29. This novel imaging approach that has made it possible to visualize the nano-spatial distribution and organization of CD44 and CD29 on MSCs may help explain the molecular mechanism behind the directional migration of MSCs induced by VEGF.

2. Materials and methods

2.1. Isolation and culture of MSCs

MSCs were prepared in a similar manner to the method described by Weiss et al. [38]. Briefly, umbilical cords were collected and processed within 12 h after normal births. Umbilical arteries and vein were removed, and the remaining tissue was transferred to a sterile container in Dulbecco's modified essential media (DMEM) containing antibiotics (penicillin 100 mg/ml, streptomycin 10 mg/ml, and amphotericin B 250 mg/ml) and cut into small fragments. The explants were transferred to 6-well plates containing DMEM supplemented with 20% fetal bovine serum. After a week, when well-developed colonies of fibroblast-like cells appeared, cultures were harvested with 0.05% trypsin and passaged onto sterilized coverslips and kept in a 6-well plate for 2–3 days.

2.2. Preparation of methyl cellulose dish (MCD)

One percent methyl cellulose (Sigma, M-0512) was dissolved with distilled water and sterilized in a high pressure sterilization pot. Three hundred microliters of 1% sterile methyl cellulose was added to mold concave hole and dried on a laminar flow cabinet. Finally, the methyl cellulose membrane was prepared and placed in aseptic petri dishes for later use.

2.3. Sample preparation

The above prepared MCDs were placed on one side of the cell culture dish, as shown in Fig. 1, while the coverslip with cells were placed on the other side of the cell culture dish (an experimental group injected with 300 μl of 50 ng/ml VEGF into the MCD, another control group injected with 300 μl of PBS). Upon adding medium, VEGF could diffuse in a gradient in the dish. After the cells were incubated for 24 h at 37 °C in a 5% CO_2 incubator, MSCs grown on the sterile coverslip were first washed three times with PBS buffer, then fixed with 4% formaldehyde at room temperature for 15 min and washed another three times with PBS prior to incubating with monoclonal antibodies (mAbs), phalloidin–FITC, and anti-human FAK.

2.4. Dual-color immunofluorescence labeling

Dual-color immunofluorescence labeling for mAbs and QD conjugates was performed according to the methods described by Chen et al. [31,32] with slight modifications. Briefly, the cells were blocked for 60 min with 6% bovine serum albumin to rule out nonspecific adsorption of biotin-CD29. The cells were incubated with 20 μg/ml biotinylated anti-human CD29 antibody for 60 min, washed three times with PBS to remove unbound CD29, followed by incubation with 1 μg/ml QD655 (red light emitting)-streptavidin for 60 min. For the second color labeling, we used 200 μg/ml biotin to block residual avidin sites on the surface of QDs before repeating the CD29 protocol with the CD44 antibody. CD44 labeling used QD565 (green light emitting)-streptavidin so that it could be distinguished from CD29. The samples destined for laser scanning confocal microscopy (LSCM) were washed three times with PBS to remove any unbound QDs and mounted on a glass slide with 30% glycerol. The samples used for NSOM were washed three times with dd water to remove any QDs and salt particles on the cells.

2.5. NSOM imaging

An Aurora-2 NSOM system (Veeco) was used in this study. The system was shown schematically in our pervious study [34]. The samples are mounted on the XY stage with a full scanning range of 30 μm × 30 μm, and a video camera was used to locate the region of interest. The excitation light came from a DPSSL laser (457 nm, Changchun Photoelectric Inc., Jilin, China) coupled with an Al-coated tapered fiber probe with an aperture diameter of approximately 50 nm. The probe tip was attached to a piezoelectric quartz tuning fork (resonance frequency of approximately 93 kHz), and the probe–sample distance was maintained constantly at 10 nm by tuning-fork-based shear-force feedback. This mode of operation provided simultaneous topographic

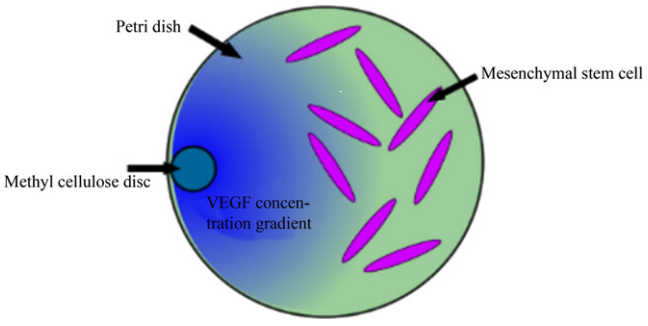

Fig. 1. A schematic diagram of experimental setup. Mesenchymal stem cells are seeded in a culture dish with a VEGF concentration gradient.

and optical data and the data were collected using a 40 × 0.65 objective (Olympus Corp., Tokyo, Japan). The collected light was filtered at 565 ± 10 nm for QD565 and 655 ± 10 nm for QD655 using a Liquid Crystal Tunable Filter (VariSpec, CRI, Inc.) to separate the fluorescence emission from the excitation light. Our previously data indicated that QDs exhibit a relatively homogeneous spread with a mean size (measured at the full width at half maximum, FWHM) of 50 nm which is a result of the convolution effect of the probe (the diameter of QD605-streptavidin is ~20 nm according to the vendor), indicating that NSOM probes were able to generate nanoscale images of the QDs and that the 50-nm dots corresponded to single QDs [32]. These results suggest that QD-based NSOM imaging may be suitable for single molecule detection on the cell surface. In this study, the laser excitation intensity was approximately 200 W/cm^2 and all images consisted of 300 × 300 measured points.

2.6. LSCM imaging

Focal adhesion formations and cytoskeletal dynamics were evaluated by labeling with anti-FAK and FITC–phalloidin. MSCs with or without VEGF stimulation were incubated separately with 50 mM anti-FAK and 1 mM FITC–phalloidin for 60 min in the dark at room temperature. After, cells were washed twice with PBS. Then, focal adhesion formation, cytoskeletal organization, and the localization of CD44 and CD29 were imaged by a LSCM (LCM 510 Meta Duo Scan, Carl Zeiss, and Germany).

2.7. AFM imaging

MSCs incubated with or without VEGF for 24 h were fixed with 2.5% glutaraldehyde for 10 min. Cells on 24-well plates were washed with distilled water three times and air-dried at room temperature. The sample was mounted onto the XY scanning station with a max scanning range of 100 μm × 100 μm and observed at room temperature by AFM (Autoprobe CP Research, Thermomicroscopes, Veeco Instruments Inc.) in contact mode. The spring constant of the Si_3N_4 cantilevers (Microlever; Park Scientific Instruments) and the radius of curvature of the tips were 2.8 N/m and 10 nm respectively. All of the acquired images (256 pixel × 256 pixel) were flattened by the provided software (IP 2.1) to eliminate background noise at low frequency in scanning direction (flattening order: 0–1).

2.8. Migration of MSCs

To analyze the migration of MSCs, we performed the wound-healing migration assay. The assay was performed as described previously [39]. Briefly, MSCs were plated onto the 24-well plates which were then cultured overnight at 37 °C in a 5% CO_2 incubator. After reaching 80%, confluence MSCs were starved to inactivate cell proliferation and a scratch was made on the cell layer using a pipette tip. DMEM-F12 containing 0.5% FBS was added in the presence or absence of VEGF. The open wound surface area was quantified with an inverted phase-contrast microscope following 0, 1, 6, 12 and 24 h incubation. All experiments were repeated at least three times.

2.9. Data processing and statistics

Confocal microscopic images were processed using Zeiss LSM software (Carl Zeiss, Germany). The NSOM data was processed by the SPMLab 5.0.1 software (Veeco, Santa Barbara, CA). The size of a fluorescent spot was defined by the maximum distance between two pixels within the contour of each spot. The intensity of each spot was defined by the sum of the intensity over all pixels within the contour of the spot. The 2-dimensional merged image of two color fluorescence images was generated using Image J. Fluorescence statistics were analyzed in a semiautomated fashion using custom-written software based on Matlab 6.5 (The Mathworks Inc., Natick, MA) and Visual C++ 6.0 (Microsoft Corp., Redmond, WA). SPSS 11.02 (SPSS Inc., Chicago, IL) was used to create histograms.

3. Results

3.1. Inverted microscope images of MSCs

To confirm the effect that a concentration gradient of VEGF has on the migration of MSCs, we used an inverted microscope to observe changes in MSC morphology at the macroscopic scale. As shown in Fig. 2A, most MSCs in the control group had a regular spindle shape indicating that they were well-spread on the coverslip and appeared randomly oriented. The cell density was also rather low. However, in the presence of a VEGF gradient, the cell density increased greatly, indicating that a large number of MSCs had proliferated. Moreover, the vast majority of MSCs had a long spindle shape and were preferentially distributed toward the top left corner, where the MCD was located (Fig. 2B). These results indicate that MSCs were migrating to the location of the MCD.

3.2. LSCM imaging of CD29 and CD44 molecules

We wanted to find out whether directed migration in MSCs is related to the two important adhesion molecules, CD44 and CD29. For this purpose, QD-based fluorescence dual-color labeling technology was used to visualize the distribution of CD29 and CD44 molecules on MSCs in the presence or absence of VEGF stimulation for either 30 min or 24 h. Green fluorescence QDs were used to label CD44, while red fluorescence QDs were used for CD29, and their locations on the cell were measured by LSCM (Fig. 3). Yellow fluorescence indicates colocalization of CD44 and CD29.

In the control group (Fig. 3A), CD44 was uniformly distributed over the cell surface and granular fluorescence could be observed. A large number of CD29 molecules were located at the edge of MSCs while a few molecules could be found on the top of cells. The merged images of CD29 and CD44 show faint colocalization.

At 30 min post-VEGF stimulation, the distribution of CD44 and CD29 (Fig. 3B) was not significantly different when compared with the control group. However, after VEGF-stimulation for 24 h (Fig. 3C), the growth of MSCs trended toward a specific direction, consistent with the results observed by an inverted microscope. The distribution of CD44 and CD29 also showed significant changes. Fig. 3C shows that, both CD44 and CD29 appeared as larger fluorescent spots. To compare their fluorescence intensity with the control group and the 30 min stimulation group, the LSCM detector gain was increased approximately 20%. These results suggest that the expression level of CD44 and CD29 was increased with increased stimulation time with VEGF. At the same time, the area of colocalization between CD44 and CD29 molecules was also increased. In order to further study the distribution and colocalization of CD44 and CD29, we used the “digital zoom” function of LSCM to enlarge the white boxed area shown in Fig. 3C (top right), and the enlarged region is shown in the lower panel of Fig. 3C. In these zoomed-in regions, larger CD44 clusters and areas of CD29 aggregation, as well as colocalization between the two adhesion molecules were more clearly visible.

3.3. In situ NSOM/QD-based dual color fluorescence imaging of CD44 and CD29 on VEGF-stimulated MSCs

As the inter-molecular distances between CD44 and CD29 are too small to be resolved by confocal imaging, we were unable to map the nanometer scale distribution of these two membrane proteins. Therefore, we performed in situ NSOM/QD-based nanoscale fluorescence imaging of CD44 and CD29 to verify the results obtained by LSCM.

Fig. 4a shows the NSOM image of control MSCs with CD44 labeled in green (Fig. 4aB) and CD29 labeled in red (Fig. 4aC). The large-scale near-

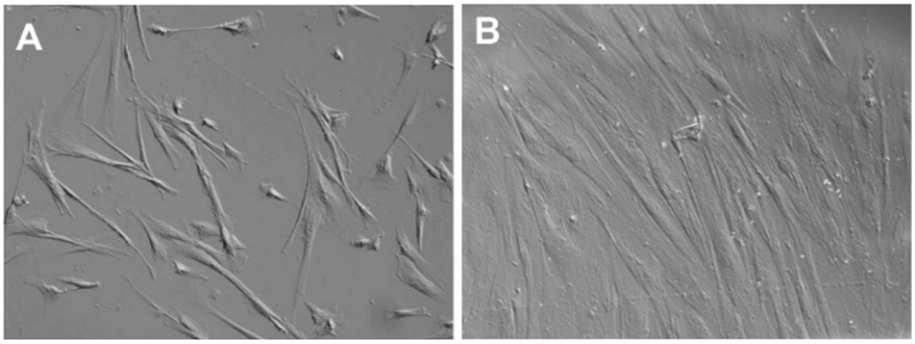

Fig. 2. Inverted microscope images of MSCs. (A) Control group and (B) induction group by VEGF for 24 h.

field fluorescence images (Fig. 4aB, C) show a number of small, well-separated domains that are randomly distributed across the cell surface. In order to quantitatively investigate the spatial organization of CD44 and CD29 molecules, the physical sizes of all the fluorescent spots in Fig. 4aB and C were calculated. The sizes of the 53 fluorescent spots in Fig. 4aB (CD44) ranged from 70 nm to nearly 330 nm, with an average

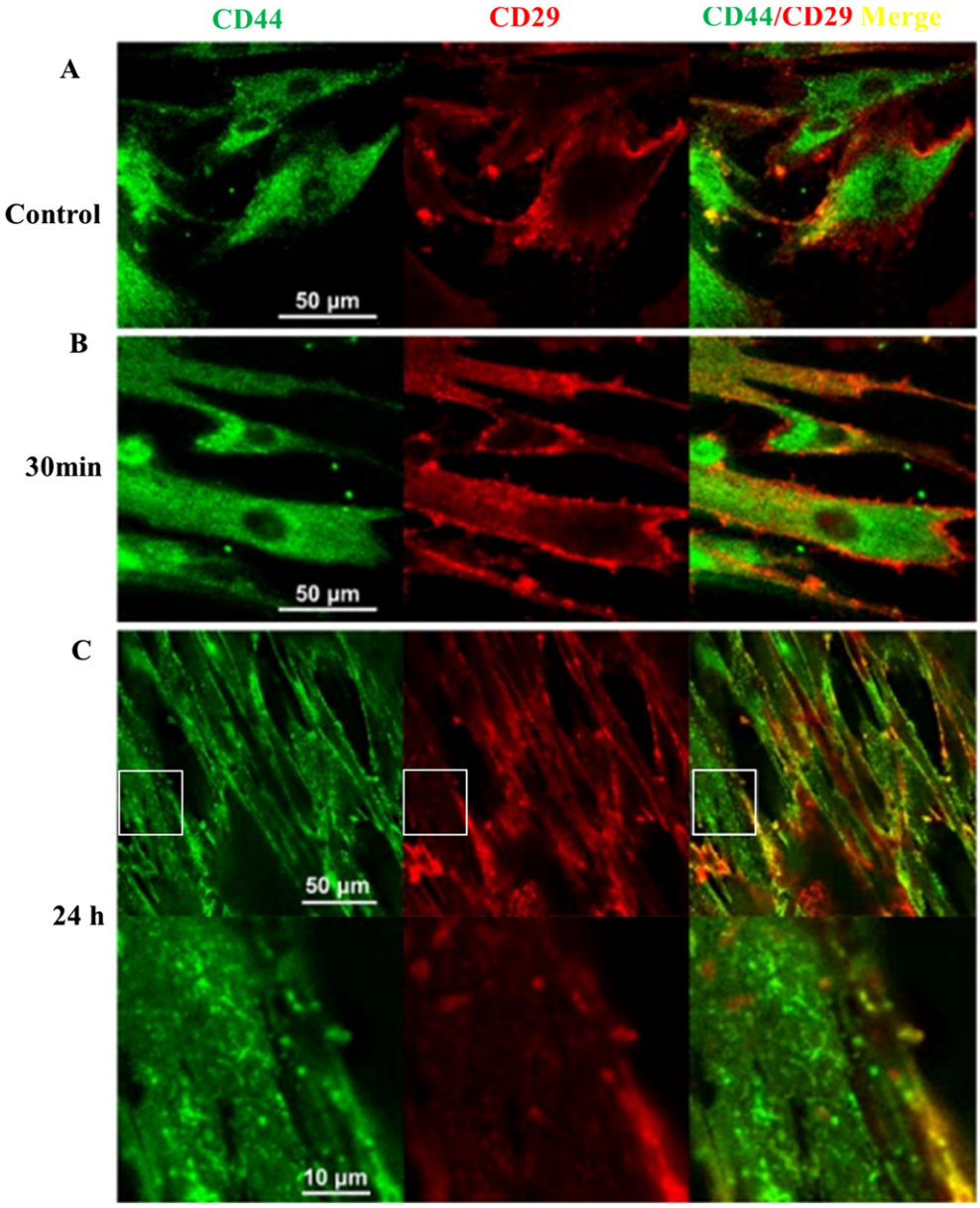

Fig. 3. Fluorescent images of CD44 and CD29 acquired by LSCM. A, Control MSCs without VEGF stimulation; B and C, MSCs stimulated with VEGF for 30 min and 24 h respectively. Cells are surfaced stained with anti-CD44 antibody (QD565, green) and anti-CD29 antibody (QD655, red). The right panel is the merged image showing overlayed CD44 and CD29. Yellow fluorescence indicates co-localization.

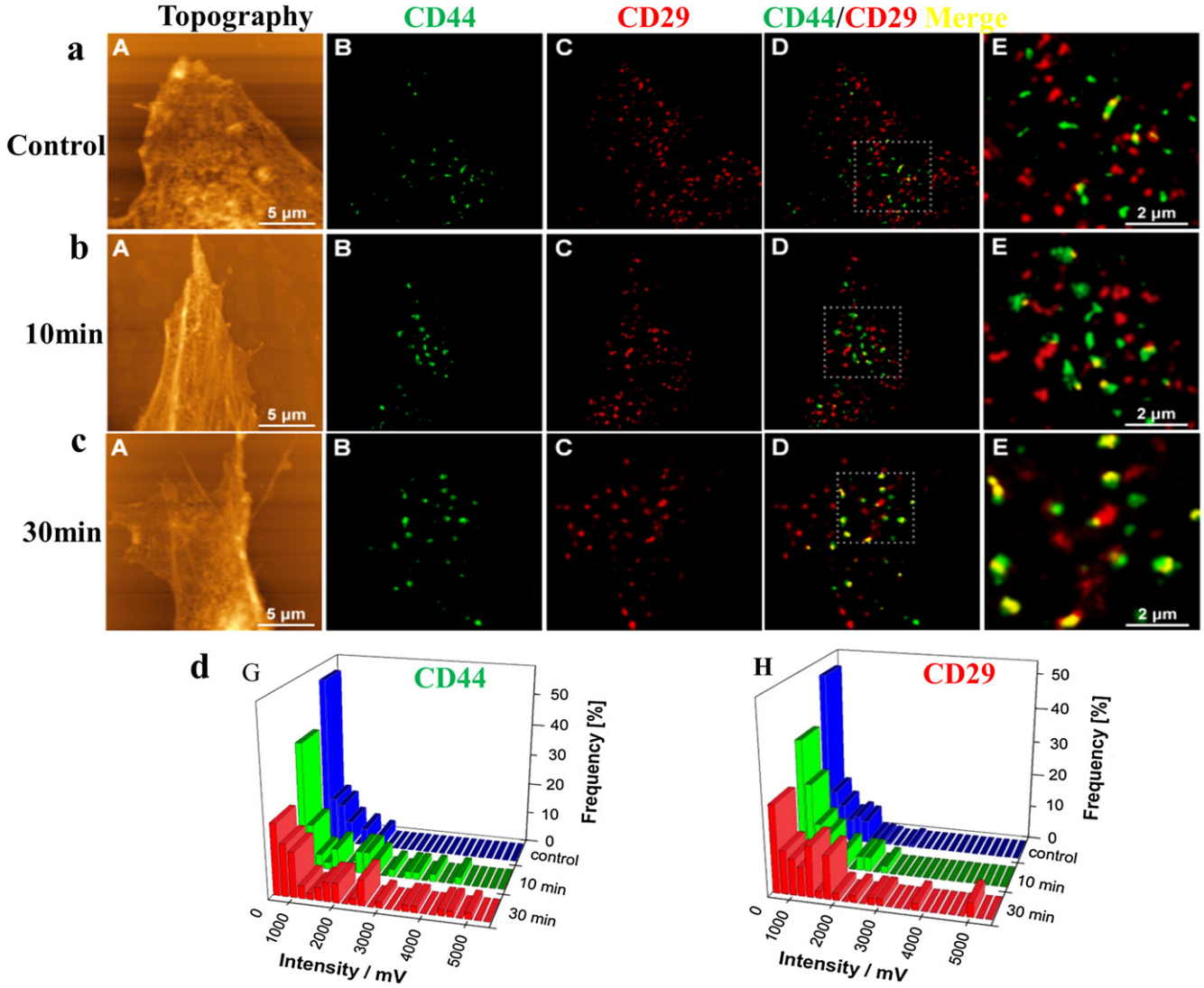

Fig. 4. In situ NSOM/QD-based dual color fluorescence imaging in MSCs induced by VEGF for 30 min. a, Control MSCs; b and c, NSOM images of MSCs after stimulation by VEGF for 10 min and 30 min respectively. (A) Topographic images of the cell surface. (B) Near-field fluorescence images of CD44 labeled using QD565. (C) Near-field fluorescence images of CD44 labeled using QD655. (D) Superimposition of (B) and (C), yellow indicates colocalization between CD44 and CD29. (E) The marked area in (D) is magnified by B-spline interpolation. Few CD44 molecules colocalize with CD29 in the merged image (a). As VEGF stimulation time increased, both CD44 and CD29 formed nanodomains or even microdomains (>500 nm) and colocalization increased between the two molecules (c). d, Histograms of the frequency distribution of all the CD44 and CD29 fluorescent spots, blue: control group; green: 10 min VEGF stimulation; and red: 30 min VEGF stimulation.

value of 200 ± 130 nm. The sizes of the 151 fluorescent spots in Fig. 4aC (CD29) ranged from less than 100 nm to 350 nm, with an average value of about 230 ± 130 nm. Fig. 4aD is a superimposed image consisting of (B, C) and (E) the marked area in (D) was magnified by B-spline interpolation. It was observed that most CD44 and CD29 molecules were randomly scattered on the cell surface and co-localization rarely occurred between CD44 and CD29.

Fig. 4b shows the MSCs that have been stimulated with VEGF for 10 min. CD44 was labeled green (Fig. 4bB) and CD29 was labeled red (Fig. 4bC). Fig. 4bA is a topographic image of the cell. Some small pseudopodia could be seen around the edge of the cell. The sizes of 42 fluorescent spots in Fig. 4bB (CD44) ranged from 163 nm to nearly 427 nm, with an average value of about 295 ± 132 nm. The sizes of 96 fluorescent spots in Fig. 4bC (CD29) ranged from 120 nm to 408 nm, with an average value of about 264 ± 144 nm. The area of co-localization between CD44 and CD29 was 0.327 μm^2.

Fig. 4c shows the NSOM image of MSCs stimulated with VEGF for 30 min. CD44 was labeled green (Fig. 4cB) and CD29 was labeled red (Fig. 4cC). Compared with the topographic images of the cell in Fig. 4aA and Fig. 4bA, there was a significant increase in the number of pseudopodia of the cell in Fig. 4cA. The sizes of 33 fluorescent spots in Fig. 4cB (CD44) ranged from 153 nm to nearly 505 nm, with an average value of approximately 329 ± 176 nm. The sizes of 48 fluorescent spots in Fig. 4cC (CD29) ranged from 153 nm to 467 nm, with an average value of approximately 310 ± 157 nm. The area of co-localization between CD44 and CD29 increased to 0.917 μm^2 (Fig. 4cD and Fig. 4cE). Therefore, the average sizes of CD44 and CD29 spots increased with the increasing VEGF stimulation, while the area of co-localization between CD44 and CD29 also increased from 0.327 μm^2 to 0.917 μm^2.

Aside from calculating the physical size of the fluorescent spots, we also analyzed the fluorescent intensity of these spots. Histograms of the frequency distribution of CD44 and CD29 fluorescence intensities are shown in Fig. 4dG and H. In Fig. 4dG, the intensity of fluorescent spots from CD44 (two cells, 130 fluorescent spots) was less than 2000 mV in the control group (blue histogram). After MSCs were stimulated for 10 min with VEGF, the intensity of more than 30% of the fluorescent spots (two cells, 101 fluorescent spots) was increased to above 2000 mV (green histogram). Following 30 min stimulation with VEGF, the intensity of 33 fluorescent spots from one cell was further increased, and 5% of the fluorescent spots showed intensities as

high as 4500 mV. However, the rate of increase after 30 min stimulation (red histogram) was lower than the 10 min stimulation. In contrast, the fluorescence intensity of CD29 in both the control group (one cell, 151 fluorescent spots) and the 10 min VEGF stimulation group (two cells, 176 fluorescent spots) was lower than 3000 mV and there were no significant changes between the two groups. This indicates that CD29 aggregation is not obvious and that there is only a subtle increase in the intensity of fluorescent spots after 10 min (Fig. 4dH). After 30 min stimulation with VEGF, the intensity of fluorescent CD29 spots (two cells, 101 fluorescent spots) increased rapidly and 5% of fluorescent spots reached 5000 mV in intensity. Together, these findings suggest that CD44 molecules first assemble the nano-domain, followed by CD29 nano-domain formation. These changes at the molecular level may contribute to the directional migration of MSCs.

3.4. Focal adhesion formation and morphological changes of MSCs induced by VEGF

Focal adhesion formation is an essential step during cell adhesion and migration. To investigate the underlying mechanism of focal adhesion formation on cell adhesion and migration induced by VEGF, immunofluorescence labeling was used to examine the effect of VEGF on the distribution and expression level of FAK, a major component of focal adhesions. Fig. 5a shows the immunofluorescence images and quantitative expression of FAK as measured by LSCM and flow cytometry. The fluorescence intensity data from LSCM images show that, following VEGF stimulation, FAK expression increased and appeared to aggregate (Fig. 5aC, D). Simultaneously, quantitative data from flow cytometry (Fig. 5aE) also indicated that the mean fluorescence intensity (MFI) of FAK increased from the control group of 900 ± 120 to 1500 ± 205 in MSCs upon VEGF treatment.

Under both phase contrast microscope and NSOM, MSCs were observed to acquire an elongated spindle-like shape, while cell adhesion molecules on MSCs formed clusters upon treatment with VEGF. To obtain more subtle morphological data, high-resolution AFM was used. In each group, more than 10 cells were analyzed and measured by AFM at the cell periphery. As shown in Fig. 5b, there were abundant pseudopodia among the VEGF-induced MSCs (Fig. 5bC), which may play a role in intracellular communication and migration. We also compared average roughness (Ra) and root-mean-square roughness (Rq) in the analytical area between the control and VEGF-treated groups (Fig. 5bE). Ra and Rq are an evaluation of the smooth degree of cell membrane. The roughness calculation of a cell surface provides novel information regarding to the effect of external stimulation on membrane topography. The topography of 1 μm × 1 μm membrane surface in the control group was shown in Fig. 5bB. By analysis, the values of Ra and Rq were 7.5 nm ± 1.0 nm and 6.2 nm ± 0.8 nm, respectively. After being treated with VEGF for 24 h (Fig. 5bD), both of them increased to 12.2 nm ± 1.5 nm (Rq) and 9.2 nm ± 1.2 nm (Ra). It would appear that as the expression and co-localization of CD29 and

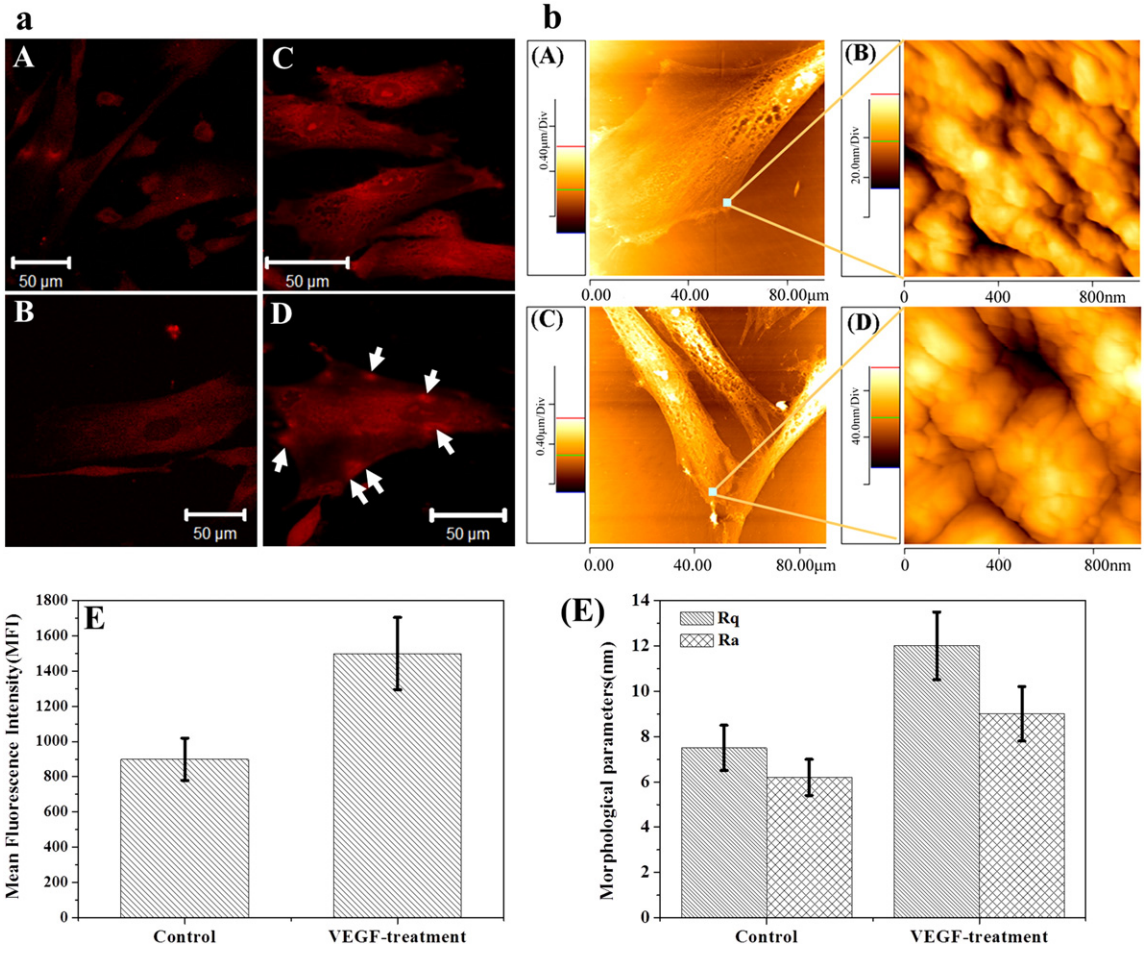

Fig. 5. a. FAK (labeled with Rhodamine anti-human FAK) as imaged by LSCM and FCM. A–D, LSCM images of FAK distribution. (A, B) are the control MSCs and (C, D) are 24 h VEGF-induced MSCs. E, Quantification of mean fluorescence intensity (MFI) of FAK in the control group and the VEGF-induced group. The data were expressed as mean ± S.D. from three independent experiments. Arrows indicate FAK aggregation. b. AFM topographical images of cell-surface ultra-structures in MSCs treated with or without VEGF. (A, B) Control MSCs and (C, D) 24 hour VEGF-induced MSCs. (A, C) 2-D images of the whole cells; (B, D) 2-D images of cell-surface areas (1 μm × μm) were enlarged from the corresponding cells on the left panel. There are many pseudopodia on the MSCs (dotted boxes). (E), Comparison of the ultra-structural parameters (Rq, Ra) between the control group and the VEGF-induced group. Ra and Rq are the average roughness and root-mean-square roughness in the analytical area, respectively. All parameters were directly generated by the software IP2.1 using 10 cells for each group.

CD44 increase at the surface of MSCs, the surface particles turned into large.

3.5. Cytoskeletal rearrangement with VEGF stimulation

To determine whether the cell movement we observed is due to cytoskeletal rearrangements, we analyzed the cellular distribution of actin by an inverted microscope (Fig. 6a) and by LCSM (Fig. 6b). Fluorescence imaging of the cytoskeleton indicated that the actin in control MSCs was disordered (Fig. 6aA and Fig. 6bA, C), while actin in VEGF stimulated cells showed an elongated spindle shape (Fig. 6aB) and enlarged regions showed well-organized cytoskeletal alignment directed toward a specific orientation (Fig. 6bB, D). These results further confirm that directed migration in MSCs is associated with cytoskeletal rearrangements.

3.6. VEGF treatment enhanced the migration of MSCs

To further confirm the ability of VEGF to induce the migration of MSCs, we performed simulated wound healing assays. After making the wound by scratching the surface of the cell culture, MSCs were incubated with or without VEGF for 0, 1, 6, 12, or 24 h before they were evaluated for their ability to migrate into the wound area using an inverted microscope. Fig. 7a shows images from the wound healing experiment. The histogram in Fig. 7b shows the number of migrated cells after treatment with VEGF at different times. These data indicate that VEGF significantly enhanced the migration of MSCs.

4. Discussion

Cells use cell surface receptors to acquire information about and to respond to their environments. Cell surface molecules regulate many essential cellular processes, including cell adhesion, tissue development, cellular communication, inflammation, tumor metastasis, and responses to microbial infection. These events often involve multimolecular interactions that take place on a nanometer scale and at very high local concentrations. Therefore, understanding molecular localization on a single-molecule scale, and its assemblies and interactions on the cell surface is an important challenge that can be difficult to address because of the lack of high-resolution single-molecule imaging techniques.

To our knowledge, the NSOM/QD-based imaging system generates the best optical resolution (50 nm) for immunofluorescence imaging of molecules on the cell surface. In this study, we used a NSOM/QD-based imaging system to directly image the spatial relationship between CD44 and CD29 on MSCs before and after stimulation with VEGF. Although confocal microscopy showed that the expression levels of CD44 and CD29 increased upon VEGF stimulation for 24 h, leading to the formation of some aggregates on the cell membrane, the technique was not able to produce nanometer-scale information regarding whether and how these molecules are distributed on the cell membrane and whether they share the same space. Most importantly, there were no obvious changes that could be detected by LSCM during a short period of stimulation. On the other hand, the NSOM/QD-based nanoscale imaging system allowed us to directly visualize the changes of molecular distribution and organization on the membrane of MSCs.

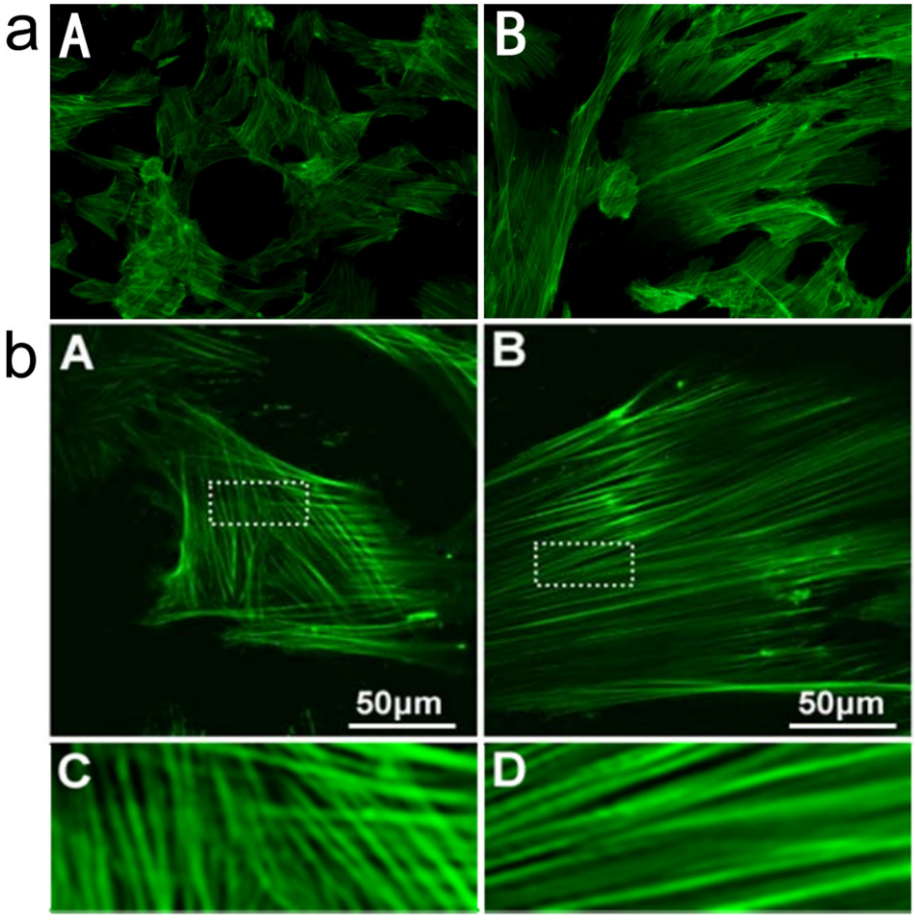

Fig. 6. Fluorescence microscopy of phalloidin staining. A and C, The representative nonaligned action structure under control conditions with detail picture (C); B and D, Aligned actin structure in the presence of VEGF with detail picture (D). a and b are respectively obtained by a common inverted fluorescence microscope (20×) and a laser confocal scanning microscope.

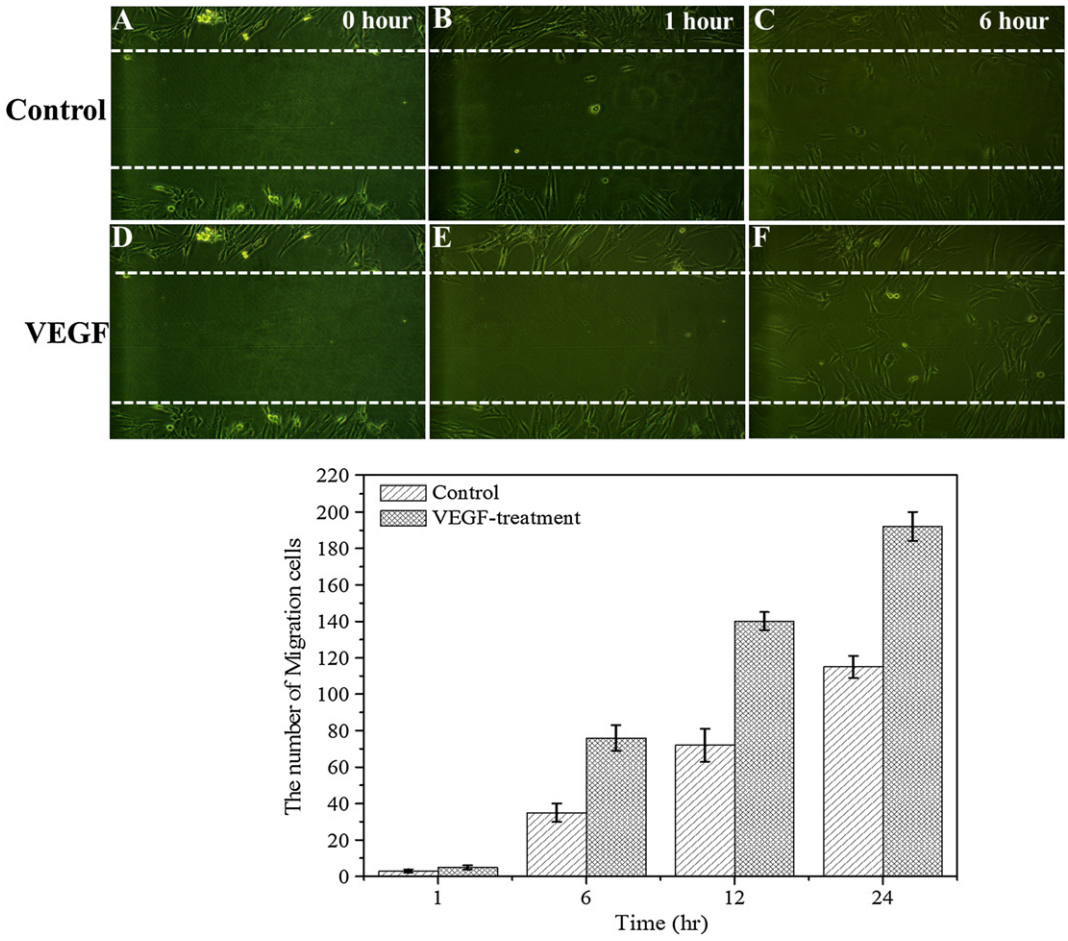

Fig. 7. Wound and healing assay with a confluent monolayer of mesenchymal stem cells. (A–F): After scratching, the surrounding cells migrated into the scratched area (time after scratching is indicated). (G) Histogram of the number of migrated cells in control and VEGF group at different times. (A–C) The control group; (D–F) VEGF-induced group.

To facilitate the evaluation of the spatial distribution and organization of CD44 and CD29, nanostructures of both molecules were classified based on their organization and their apparent size by immunofluorescence: (i) nano-clusters, <200 nm, (ii) nano-domains, >200 but <500 nm, and (iii) micro-domains, >500 nm. The scale is adapted from Chen et al. [35]. To our surprise, both the analyses of intensity and size confirmed that over 30% of CD44 molecules rapidly form nano-domains that increased significantly in size from 200 nm to 295 nm and that increased significantly in intensity from below 2000 mV to above 2000 mV. These changes were clearly observed by NSOM as early as 10 min after VEGF stimulation. As the time of VEGF stimulation was increased, some of the CD44 molecules even formed micro-domains. This phenomenon was also confirmed by results obtained by LSCM (Fig. 4).

Cell surface CD44 glycoproteins bind to HA and other glycosaminoglycans and mediate cell adhesion to and migration through the extracellular matrix. Through its interaction with proteins that bind to actin microfilaments, CD44 serves as a linkage that transmits signals from the cell surface to the cytoplasm. In many of these events, the engagement of CD44 induces lipid raft reorganization, which has been suggested to promote the formation of specialized membrane microdomains containing multiple signaling molecules assembled in complexes that promote the efficient transduction of sustained signals. In addition, CD44 acts as the co-receptor of VEGFR-2, which plays an important role in mediating intracellular signal transduction [30]. It has been reported that hMSCs express VEGFR-2 abundantly and stably [26]. Our results support the idea that once VEGF is bound to VEGFR-2 on MSCs, CD44 molecules are activated by VEGF, which helps further induce lipid raft reorganization to form larger area lipid rafts. In turn, CD44 molecules located in lipid rafts become part of the larger aggregation. Although similar reports indicate that binding-induced lateral redistribution of CD44 into lipid rafts can be clearly observed as early as 30 min after Ab-mediated cross-linking [29], our results show that these changes take place much sooner than reported.

Our NSOM imaging clearly shows that the VEGF-induced activation of CD29 takes place after the activation of CD44, which was shown by an increase in fluorescence intensity and dot size of CD29 molecules when VEGF stimulation was increased to 30 min. Our model for this finding is as follows. Firstly, VEGF exerts its effects by binding to the receptor tyrosine kinase VEGFR-2. Tyrosine phosphorylation of VEGFR-2 at residue Y951 facilitates the binding of VEGFR-2 to the Rous sarcoma (Src) homology 2-domain of the T cell-specific adaptor (TSAD), which in turn regulates VEGF-induced activation of the c-Src tyrosine kinase [40]. Then, CD44 molecules, acting as co-receptors of VEGFR-2, are activated by VEGF and further induce lipid raft reorganization to form the larger area lipid rafts. This results in the recruitment of more Src to the lipid raft [29]. Finally, integrin (CD29) aggregation is most likely promoted by a combination of Src and CD29, as Src family molecules are one of the ligands of integrins. Most importantly, there is an increased amount of co-localization between CD44 and CD29 after VEGF stimulation for 30 min, which further suggests that both CD44 and CD29 are located in the newly formed lipid rafts. CD44–Src is brought within close proximity to integrins and triggers integrin activation. The perturbation of the lipid bilayer and associated membrane proteins during receptor engagement may facilitate the formation of larger raft

structures with longer half-lives, similar to that which is found in T-cell immunological synapses. All of these changes involving the cell membrane were detected by AFM (Fig. 5b). Our ultra-structural images found that the membrane in the control group was much smoother than in the VEGF-induced group.

Focal adhesion kinase (FAK) is a crucial signaling component that is activated by numerous stimuli and functions as a biosensor or integrator to control cell motility [41,42]. FAK can influence the cytoskeletal structures of cell adhesion sites and membrane protrusions to regulate cell movement [43,44]. Therefore, observing the effects of VEGF on FAK may be very important for understanding the underlying mechanisms behind MSC migration. Our results indicate that the level of FAK expression was not only increased, but that FAK also formed aggregations on the cell membrane following VEGF stimulation (Fig. 5a). FAK phosphorylates Cdc42-activated N-WASP at Tyr256, and causes phosphorylated N-WASP to remain in the cytoplasm where it can affect ARP2/3-mediated actin polymerization. Through associations with Rho GTPase-activating proteins (GAPs) and Rho guanine nucleotide-exchange factors (GEFs), FAK can regulate actomyosin stress fiber polymerization [44]. In our study, the VEGF-induced morphological changes in cell shape that we observed, such as cell elongation, filopodium generation, and cytoskeletal rearrangement are essential for cell migration, indicating that VEGF has significant positive effects on the migration of MSCs.

Taken together, based on our NSOM imaging analysis and literature search, we infer that the migration of MSCs toward tumor sites or region of myocardial infarction is closely associated with the interaction between VEGF and the activation of MSCs (Fig. 8). Although other experiments including immunoblotting and co-immunoprecipitation must be performed to further confirm our inference, the NSOM/QD-based imaging technique, with its diffraction-unlimited spatial resolution, has shed new light on the relationship between molecular localization and function and has provided us with detailed insights into the mechanisms of VEGF-induced cell adhesion molecule interactions at the molecule level. Indeed, NSOM is a powerful, sensitive tool with which the distribution of single molecules on cell surfaces can be imaged, providing new insight into the highly sophisticated functions of cell surface molecules.

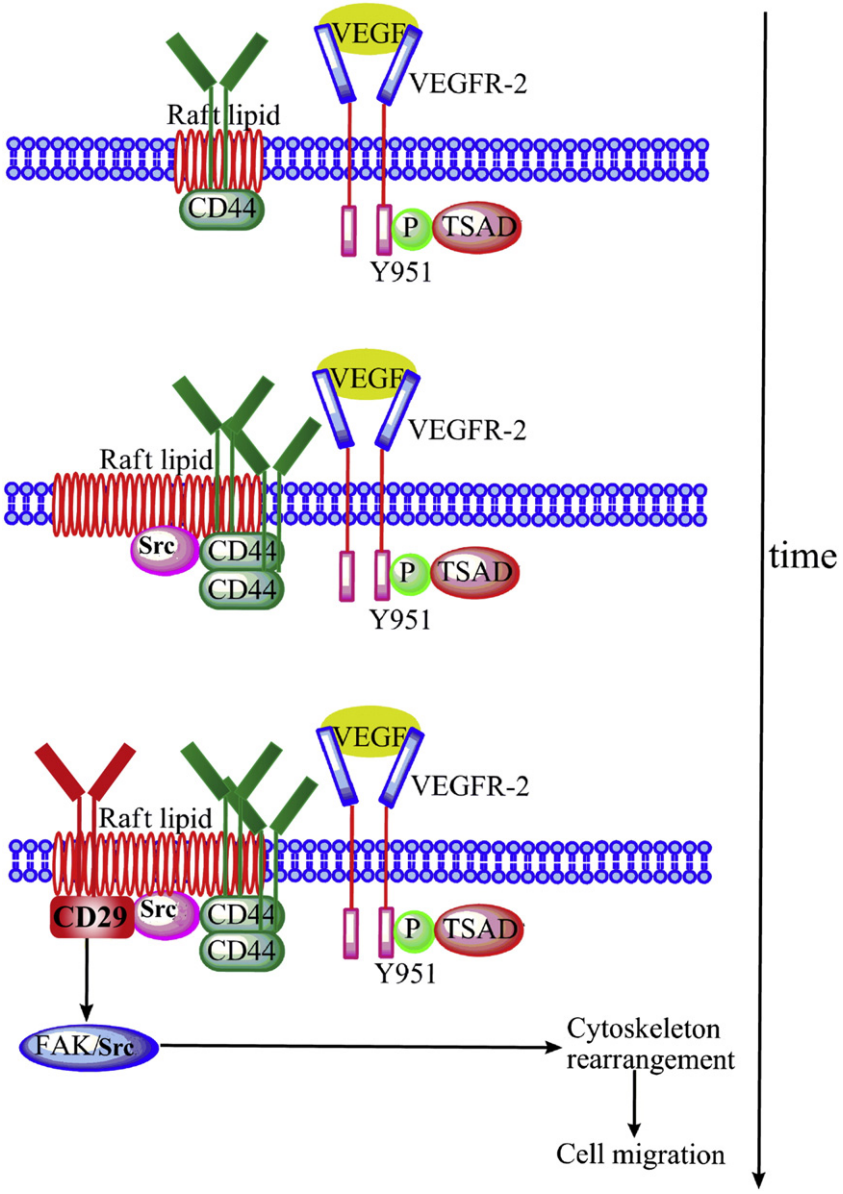

Fig. 8. A possible mechanism interaction between VEGF, CD44, and CD29 obtained from NSOM imaging and LSCM analyses.

Acknowledgements

This work was supported by research grants from Science and Technology 973 Program, China (No. 2010CB833603).

References

[1] M.F. Pittenger, Multilineage potential of adult human mesenchymal stem cells, Science 284 (1999) 143–147.
[2] T. Sun, B.C. Sun, C.S. Ni, X.L. Zhao, X.H. Wang, S. Qie, D.F. Zhang, Q. Gu, H. Qi, N. Zhao, Pilot study on the interaction between B16 melanoma cell-line and bone-marrow derived mesenchymal stem cells, Cancer Lett. 263 (2008) 35–43.
[3] S. Zhang, Y.Z. Jiang, W. Zhang, L. Chen, T. Tong, W. Liu, Q. Mu, H. Liu, J. Ji, H.W. Ouyang, X. Zou, Neonatal desensitization supports long-term survival and functional integration of human embryonic stem cell-derived mesenchymal stem cells in rat joint cartilage without immunosuppression, Stem Cells Dev. 22 (2012) 90–101.
[4] R. Barzilay, E. Melamed, D. Offen, Introducing transcription factors to multipotent mesenchymal stem cells: making transdifferentiation possible, Stem Cells 27 (2009) 2509–2515.
[5] S.A. Iqbal, C. Manning, F. Syed, V. Kolluru, M. Hayton, S. Watson, A. Bayat, Identification of mesenchymal stem cells in perinodular fat and skin in Dupuytren's disease: a potential source of myofibroblasts with implications for pathogenesis and therapy, Stem Cells Dev. 21 (2012) 609–622.
[6] J.A. Kode, S. Mukherjee, M.V. Joglekar, A.A. Hardikar, Mesenchymal stem cells: immunobiology and role in immunomodulation and tissue regeneration, Cytotherapy 11 (2009) 377–391.
[7] A. Schmidt, D. Ladage, T. Schinköthe, U. Klausmann, C. Ulrichs, F.J. Klinz, K. Brixius, S. Arnhold, B. Desai, U. Mehlhorn, R.H.G. Schwinger, P. Staib, K. Addicks, W. Bloch, Basic fibroblast growth factor controls migration in human mesenchymal stem cells, Stem Cells 24 (2006) 1750–1758.
[8] A.R. Williams, B. Trachtenberg, D.L. Velazquez, I. McNiece, P. Altman, D. Rouy, A.M. Mendizabal, P.M. Pattany, G.A. Lopera, J. Fishman, J.P. Zambrano, A.W. Heldman, J.M. Hare, Intramyocardial stem cell injection in patients with ischemic cardiomyopathy: functional recovery and reverse remodeling, Circ. Res. 108 (2011) 792–796.
[9] L.C. Amado, A.P. Saliaris, K.H. Schuleri, M. St John, J.S. Xie, S. Cattaneo, D.J. Durand, T. Fitton, J.Q. Kuang, G. Stewart, S. Lehrke, W.W. Baumgartner, B.J. Martin, A.W. Heldman, J.M. Hare, Cardiac repair with intramyocardial injection of allogeneic mesenchymal stem cells after myocardial infarction, Proc. Natl. Acad. Sci. U S A. 102 (2005) 11474–11479.
[10] M.B. Pittenger MF, Mesenchymal stem cells and their potential as cardiac therapeutics, Circ. Res. 95 (2004) 9–20.
[11] V. Russo, S. Young, A. Hamilton, B.G. Amsden, L.E. Flynn, Mesenchymal stem cell delivery strategies to promote cardiac regeneration following ischemic injury, Biomaterials 35 (2014) 3956–3974.
[12] R.M. Dwyer, S.M. Potter-Beirne, K.A. Harrington, A.J. Lowery, E. Hennessy, J.M. Murphy, F.P. Barry, T. O'Brien, M.J. Kerin, Monocyte chemotactic protein-1 secreted by primary breast tumors stimulates migration of mesenchymal stem cells, Clin. Cancer Res. 13 (2007) 5020–5027.
[13] N. Hata, N. Shinojima, J. Gumin, R. Yong, F. Marini, M. Andreeff, F.F. Lang, Platelet-derived growth factor BB mediates the tropism of human mesenchymal stem cells for malignant gliomas, Neurosurgery 66 (2010) 144–157.
[14] S. Xu, E. Menu, A.D. Becker, B. Van Camp, K. Vanderkerken, I. Van Riet, Bone marrow-derived mesenchymal stromal cells are attracted by multiple myeloma cell-produced chemokine CCL25 and favor myeloma cell growth in vitro and in vivo, Stem Cells 30 (2012) 266–279.
[15] Z. Gao, L. Zhang, J. Hu, Y. Sun, Mesenchymal stem cells: a potential targeted-delivery vehicle for anti-cancer drug, loaded nanoparticles, Nanomedicine-Nanotechnol. Biol. Med. 9 (2013) 174–184.
[16] B. Hall, M. Andreeff, F. Marini, The participation of mesenchymal stem cells in tumor stroma formation and their application as targeted-gene delivery vehicles, Handb. Exp. Pharmacol. (2007) 263–283.
[17] A.E. Karnoub, A.B. Dash, A.P. Vo, A. Sullivan, M.W. Brooks, G.W. Bell, A.L. Richardson, K. Polyak, R. Tubo, R.A. Weinberg, Mesenchymal stem cells within tumour stroma promote breast cancer metastasis, Nature 449 (2007) 557–563.
[18] J. Kim, R.A. Denu, B.A. Dollar, L.E. Escalante, J.P. Kuether, N.S. Callander, F. Asimakopoulos, P. Hematti, Macrophages and mesenchymal stromal cells support survival and proliferation of multiple myeloma cells, Br. J. Haematol. 158 (2012) 336–346.
[19] P.J. Mishra, J.W. Glod, D. Banerjee, Mesenchymal stem cells: flip side of the coin, Cancer Res. 69 (2009) 1255–1258.
[20] X.L. Yan, C.J. Fu, L. Chen, J.H. Qin, Q. Zeng, H.F. Yuan, X. Nan, H.X. Chen, J.N. Zhou, Y.L. Lin, X.M. Zhang, C.Z. Yu, W. Yue, X.T. Pei, Mesenchymal stem cells from primary breast cancer tissue promote cancer proliferation and enhance mammosphere formation partially via EGF/EGFR/Akt pathway, Breast Cancer Res. Treat. 132 (2011) 153–164.
[21] H.F. Zhao, J. Chen, Z.S. Xu, K.Q. Zhang, Distribution and differentiation of mesenchymal stem cells in tumor tissue, Chin. Med. J.(Engl) 122 (2009) 712–715.
[22] I.A.W. Ho, K.Y.W. Chan, W.-H. Ng, C.M. Guo, K.M. Hui, P. Cheang, P.Y.P. Lam, Matrix metalloproteinase 1 is necessary for the migration of human bone marrow-derived mesenchymal stem cells toward human glioma, Stem Cells 27 (2009) 1366–1375.
[23] K. Wakabayashi, A. Nagai, A.M. Sheikh, Y. Shiota, D. Narantuya, T. Watanabe, J. Masuda, S. Kobayashi, S.U. Kim, S. Yamaguchi, Transplantation of human mesenchymal stem cells promotes functional improvement and increased expression of neurotrophic factors in a rat focal cerebral ischemia model, J. Neurosci. Res. 88 (2009) 1017–1025.
[24] Z.Y. Bian, G. Li, Y.K. Gan, Y.Q. Hao, W.T. Xu, T.T. Tang, Increased number of mesenchymal stem cell-like cells in peripheral blood of patients with bone sarcomas, Arch. Med. Res. 40 (2009) 163–168.
[25] C. Schichor, T. Birnbaum, N. Etminan, O. Schnell, S. Grau, S. Miebach, K. Aboody, C. Padovan, A. Straube, J.C. Tonn, R. Goldbrunner, Vascular endothelial growth factor A contributes to glioma-induced migration of human marrow stromal cells (hMSC), Exp. Neurol. 199 (2006) 301–310.
[26] V. Aldridge, A. Garg, N. Davies, D.C. Bartlett, J. Youster, H. Beard, D.P. Kavanagh, N. Kalia, J. Frampton, P.F. Lalor, P.N. Newsome, Human mesenchymal stem cells are recruited to injured liver in a β1-integrin and CD44 dependent manner, Hepatology 56 (2012) 1063–1073.
[27] N. Foger, R. Marhaba, M. Zoller, Involvement of CD44 in cytoskeleton rearrangement and raft reorganization in T cells, J. Cell Sci. 114 (2001) 1169–1178.
[28] J.L. Lee, M.J. Wang, P.R. Sudhir, J.Y. Chen, CD44 engagement promotes matrix-derived survival through the CD44–SRC–integrin axis in lipid rafts, Mol. Cell. Biol. 28 (2008) 5710–5723.
[29] M. Tremmel, A. Matzke, I. Albrecht, A.M. Laib, V. Olaku, K. Ballmer-Hofer, G. Christofori, M. Heroult, H.G. Augustin, H. Ponta, V. Orian-Rousseau, A CD44v6 peptide reveals a role of CD44 in VEGFR-2 signaling and angiogenesis, Blood 114 (2009) 5236–5244.
[30] L. Zhong, Z. Zhang, X. Lu, D. Huang, C.Y. Chen, R. Wang, Z.W. Chen, NSOM/QD-based fluorescence–topographic image fusion directly reveals nano-spatial peak–valley polarities of CD69 and CD71 activation molecules on cell-membrane fluctuations during T-cell activation, Immunol. Lett. 140 (2011) 44–51.
[31] J. Chen, Y. Pei, Z. Chen, J. Cai, Quantum dot labeling based on near-field optical imaging of CD44 molecules, Micron 41 (2010) 198–202.
[32] J. Chen, Y. Wu, C. Wang, J. Cai, Nanoscale organization of CD4 molecules of human T helper cell mapped by NSOM and quantum dots, Scanning 30 (2008) 448–451.
[33] Y. Chen, J. Qin, Z.W. Chen, Fluorescence–topographic NSOM directly visualizes peak–valley polarities of GM1/GM3 rafts in cell membrane fluctuations, J. Lipid Res. 49 (2008) 2268–2275.
[34] Y. Chen, L. Shao, Z. Ali, J. Cai, Z.W. Chen, NSOM/QD-based nanoscale immunofluorescence imaging of antigen-specific T-cell receptor responses during an in vivo clonal V 2 V 2 T-cell expansion, Blood 111 (2008) 4220–4232.
[35] T.S. van Zanten, A. Cambi, M. Koopman, B. Joosten, C.G. Figdor, M.F. Garcia-Parajo, Hotspots of GPI-anchored proteins and integrin nanoclusters function as nucleation sites for cell adhesion, Proc. Natl. Acad. Sci. 106 (2009) 18557–18562.
[36] G. Zeng, C.Y. Chen, D. Huang, S. Yao, R.C. Wang, Z.W. Chen, Membrane-bound IL-22 after de novo production in tuberculosis and anti-mycobacterium tuberculosis effector function of IL-22$^+$ CD4$^+$ T cells, J. Immunol. 187 (2011) 190–199.
[37] M.L. Weiss, S. Medicetty, A.R. Bledsoe, R.S. Rachakatla, M. Choi, S. Merchav, Y. Luo, M.S. Rao, G. Velagaleti, D. Troyer, Human umbilical cord matrix stem cells: preliminary characterization and effect of transplantation in a rodent model of Parkinson's disease, Stem Cells 24 (2006) 781–792.
[38] X. Pang, Z. Yi, X. Zhang, B. Sung, W. Qu, X. Lian, B.B. Aggarwal, M. Liu, Acetyl-11-keto-beta-boswellic acid inhibits prostate tumor growth by suppressing vascular endothelial growth factor receptor 2-mediated angiogenesis, Cancer Res. 69 (2009) 5893–5900.
[39] Z. Sun, X. Li, S. Massena, S. Kutschera, N. Padhan, L. Gualandi, V. Sundvold-Gjerstad, K. Gustafsson, W.W. Choy, G. Zang, M. Quach, L. Jansson, M. Phillipson, M.R. Abid, A. Spurkland, L. Claesson-Welsh, VEGFR2 induces c-Src signaling and vascular permeability in vivo via the adaptor protein TSAd, J. Exp. Med. 209 (2012) 1363–1377.
[40] Y.W. Su, G.E. Besner, Heparin-binding EGF-like growth factor (HB-EGF) promotes cell migration and adhesion via focal adhesion kinase, J. Surg. Res. 189 (2014) 222–231.
[41] J. Zhang, R.M. Ren, X.F. Luo, P. Fan, X.H. Liu, S.S. Liang, L. Ma, P. Yu, H. Bai, A small physiological electric field mediated responses of extravillous trophoblasts derived from HTR8/SVneo cells: involvement of activation of focal adhesion kinase signaling, PLoS ONE 9 (2014).
[42] S.R. Coyer, A. Singh, D.W. Dumbauld, D.A. Calderwood, S.W. Craig, E. Delamarche, A.J. Garcia, Nanopatterning reveals an ECM area threshold for focal adhesion assembly and force transmission that is regulated by integrin activation and cytoskeleton tension, J. Cell Sci. 125 (2012) 5110–5123.
[43] B. Xu, Y. Ju, G. Song, Role of p38, ERK1/2, focal adhesion kinase, RhoA/ROCK and cytoskeleton in the adipogenesis of human mesenchymal stem cells, J. Biosci. Bioeng. 117 (2014) 624–631.
[44] B.K.K. Teo, S.T. Wong, C.K. Lim, T.Y.S. Kung, C.H. Yap, Y. Ramagopal, L.H. Romer, E.K.F. Yim, Nanotopography modulates mechanotransduction of stem cells and induces differentiation through focal adhesion kinase, ACS Nano 7 (2013) 4785–4798.